Automated Georegistration of High-Resolution Satellite Imagery using a RPC Model with Airborne Lidar Information

Jaehong Oh, Changno Lee, Yangdam Eo, and James Bethel

Abstract

A large amount high-resolution satellite imagery (HRSI) has been available in the commercial market because of its value in creating accurate base maps for various applications. As massive amounts of HRSI are acquired globally by satellites with short revisit times, automated but accurate georegistration is still required despite advances in precise orbit tracking and estimation. Motivated by the attractive properties of airborne lidar data, such as their high resolution and accuracy, this study proposes a new automated method for refining the HRSI with rational polynomial coefficients (RPCs) using airborne lidar information. By projecting the lidar intensity return into the HRSI space, the image matching complexity is reduced to a simple, 2D case. The true challenge is in overcoming the difference between the HRSI and the lidar intensity return to allow for reliable matching. To this end, this paper proposes a new method based on simple relative edge cross correlation (RECC) with a screening method to prevent false matching. To make the approach more robust, data snooping was added for a final detection of outliers. Experiments were performed using three Kompsat-2 images and the potential of the approach was confirmed, showing sub-pixel accuracy.

Introduction

The last decade has seen major breakthroughs in geospatial image technology in the spaceborne domain. High-resolution Earth observing (EO) satellites have shown the capability of acquiring high spatial- and temporal-resolution imagery with large swath widths such that efficient and accurate topographic mapping is enabled. Moreover, high-resolution satellite imagery (HRSI) provides a valuable base map for various applications, such as change detection, frequency monitoring of global water and climate evolution, as well as for locational purposes such as Google™ Maps (Lee *et al.*, 2011), automobile navigation, and intelligent transportation systems. Many high-resolution EO satellites are currently in operation (Oh *et al.*, 2010).

Because the data acquisition capability of EO satellites produces substantial amounts of geospatial imagery, automated but accurate georegistration of HRSI has become critical. HRSI georegistration assigns accurate geodetic or map coordinates to the pixels of the geospatial images, and therefore permits topographic mapping, target monitoring, and multitemporal data analysis from accurate image fusion. Conventional manual georegistration using GPS-surveyed ground control points (GCPS) ensures high geospatial accuracy, but it is time consuming and cost ineffective (Zhang *et al.*, 2000). There have been many studies to automate geospatial image georegistration (i.e., "target" images) by image matching to existing ground control data sources (i.e., "reference" images) (Bentoutou *et al.*, 2005; Cariou and Chehdi, 2008; Fonseca and Manjunath, 1996; Habib *et al.*, 2005; Hild, 2001; Kim and Im, 2003; Moigne *et al.*, 2006; Oh *et al.*, 2010; Ton and Jain, 1989; Shi and Shaker, 2006; Wong and Clausi, 2007; Choi *et al.*, 2011). Automatic registration software, such as Autosync in ERDAS Imagine®, is also available off-the-shelf. The typical automated image georegistration approach consists of four steps:

1. Feature identification from the target and reference.
2. Feature matching with outlier removal.
3. Establishment of the sensor model parameters.
4. Image resampling, if needed.

Among the procedures, feature extraction and matching are the most critical steps, and the strategies used to accomplish them can vary depending on the data used. Various types of data such as maps (Dowman *et al.*, 1996; Hild, 2001), pre-georegistered satellite images (Wong and Clausi, 2007), stereo satellite images (Oh *et al.*, 2011), and lidar (Abedini *et al.*, 2008; Habib *et al.*, 2005; Lee *et al.*, 2011)) were investigated to evaluate their potential as reference information. Different image-matching strategies were also tested; these included, area-based matching (Cariou and Chehdi, 2008; Chen *et al.*, 2003), point-feature matching (Abedini *et al.*, 2008; Bentoutou *et al.*, 2003; Ton and Jain, 1989; Zhang *et al.*, 2000; Li *et al.*, 2009), line-feature matching (Habib *et al.*, 2005; Shi and Shaker, 2006), planar feature matching (Mwafag, 2006), polygonal feature matching (Dowman *et al.*, 1996), and 3D wireframe use (Schickler, 1994).

Jaehong Oh is with the Electronics and Telecommunications Research Institute, 138 Gajeong-dong, Yuseong-gu, Daejeon, 305–700, Korea.

Changno Lee is with the Seoul National University of Science & Technology, 172 Gongreung 2-dong, Nowon-gu, Seoul 139–743, Korea (changno@seoultech.ac.kr).

Yangdam Eo is with the Department of Advanced Technology Fusion, Konkuk University, 1 Hwayang-dong, Gwangjin-gu, Seoul 143-1, Korea.

James Bethel is with The School of Civil Engineering, Purdue University, West Lafayette, IN 47907.

Photogrammetric Engineering & Remote Sensing
Vol. 78, No. 10, October 2012, pp. 1045–1056.

0099-1112/12/7810–1045/$3.00/0

In contrast to conventional lower-accuracy 2D georegistration, HRSI requires accurate 3D ground control information. This is because typical HRSI spatial resolution ranges from 50 cm to a few meters. Of the existing, archival data, a combination of ortho-rectified imagery and a digital elevation model (DEM) is a popular choice for 3D ground control information. However, one problem with this combination of ground control information is that it can be significantly corrupted by relief displacement. A further problem is occlusion in the reference image caused by objects on the ground, such as buildings and trees. These issues remain unresolved unless the objects are also ortho-rectified, which is called "true" orthorectification. Note that it is a labor-intensive and costly task to generate true orthoimages over a large area because of the production costs involved in the development of a DEM with accurate breaklines. Therefore, this study proposes the use of intensity return information from airborne lidar data as ground control reference data.

Airborne lidar data not only have high 3D positional accuracy, but also there is no relief displacement. Furthermore, data from lidar point clouds include the intensity of the returned signal in the near-infrared band of the electromagnetic spectrum. Airborne lidar positional accuracy can range from 15 to 30 cm (roughly less than half a pixel of HRSI) depending on the error budgets and GPS/INS systems used. In addition to these attractive properties, a large amount of lidar data has been acquired for various applications such as topographic mapping, flood hazard assessment, and coastal monitoring. In the United States, multiple agencies including USGS, NGA, FEMA, US Army Corps of Engineers, NOAA, and NRCS have collaborated to build a national lidar data set (Stoker *et al.*, 2008). Outside of the US, other countries have also made an effort to acquire lidar data. For example, The Netherlands held a nationwide lidar data collection campaign about a decade ago, and the elevation map was updated in 2010. Denmark also completed its national lidar dataset in 2008.

Use of airborne lidar data as ground control information for aerial image registration (Abedini *et al.*, 2008; Habib *et al.*, 2005), and data fusion of lidar and satellite images (Guo and Yasuoka, 2002; Kim and Muller, 2002; Sohn and Dowman, 2007) has been investigated. While airborne lidar data show great potential as reference material for automatic georegistration of HRSI, few studies have utilized available lidar intensity information for satellite image registration.

The basic idea of the strategy proposed in this paper is that the HRSI georegistration problem can be simplified to a 2D image georegistration problem by projecting the lidar point cloud with its known 3D ground coordinates to the HRSI space using available support data such as rational polynomial coefficients (RPCs). The equations used are the well-known RPC ground-to-image projection equations (Dial and Grodecki, 2002; Fraser and Hanley, 2005). Throughout this paper, the lidar intensity return image generated by lidar point-cloud projection will be called a high-resolution lidar intensity return image (HRLI). Note that, in this context, the term "high resolution" implies that the HRLI is of the same spatial resolution as the HRSI. However, the HRLI also represents the incorrectly georegistered lidar intensity return image because it is generated by the available yet often erroneous RPCs. Therefore, the correct position should be searched for by image matching to the HRSI. This is, however, the most challenging step in our proposed strategy because there will be spatial and spectral discrepancies between the HRLI and HRSI. Note that the wavelength used in most lidar systems is 1,064 nm, which is in the near-infrared band of the electromagnetic spectrum; this is slightly outside of the HRSI spectral range for a panchromatic image. Unfortunately, this spectral difference often leads to failure of the conventional area-based matching. This paper therefore proposes a new image-matching method, named relative edge cross correlation (RECC), to overcome the image discrepancy caused by the heterogeneous HRSI/HRLI data combination. Finally, the robust image matching between HRLI and HRSI enables correction of the support data (RPCs or physical parameters) for accurate georegistration.

Experiments were carried out using three panchromatic Kompsat-2 images of one meter spatial resolution and 15 km swath width. The HRLI covering almost the entire HRSI region was generated by RPC-projecting the airborne lidar, and was followed by RECC matching for the RPC refinement parameters. Affine and polynomial-based RPC correction models were tested using a final outlier check procedure, and the experiment showed about one-pixel accuracy at the checkpoints distributed over all the images.

The paper is structured as follows. In the next Section, the proposed method is explained, followed by the generation of the HRLI, and the method of utilizing HRLI for HRSI georegistration. The robust image matching, consisting of edge-matching and outlier-removal techniques, is also presented. The results and analysis of the experiment are presented followed by Conclusions.

Proposed Method

A flowchart of the proposed method is presented in Figure 1. The input data are HRSI and their RPCs along with reference data are in the form of airborne lidar data over the target area. First, the lidar data are projected into the HRSI space using the provided RPCs. This is followed by rasterization of the projected lidar data to form the HRLI, which as previously mentioned, is the lidar intensity return image. Image patches around matching points from the HRLI and HRSI are extracted and then matched based on the proposed edge-matching technique, namely RECC. RECC is complemented by

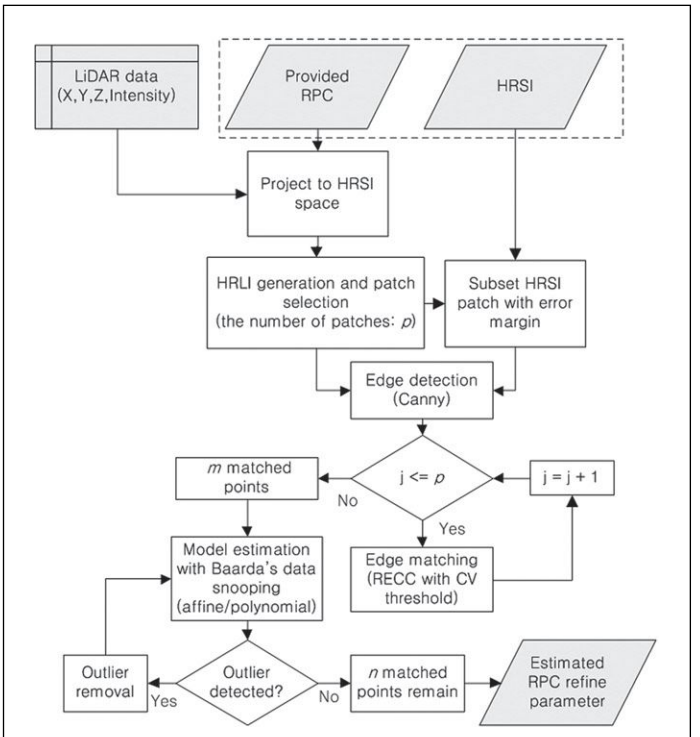

Figure 1. Flowchart of the proposed method.

concentration value (CV) computation to determine if the RECC-based matching results can be trusted for reliability. After the matching of all p patch pairs, m points are assumed to be successfully matched and are used to estimate the RPC refinement parameters such as affine or polynomials. Note that the image georegistration is simplified to a 2D problem because of the projection of the lidar data into the HRSI space. During the RPC refinement parameter estimation, the final outlier check is carried out based on Baarda's data snooping (Baarda, 1968). The procedure is performed iteratively until no outlier is detected. Finally, the remaining n out of m matching points that survive all the iterations are used for the RPC refinement parameter estimation.

Projection of Lidar to the HRSI Space for HRLI Generation

The rational function model (RFM) is the most widely used replacement sensor model for HRSI, because HRSI vendors provide its coefficients (i.e., the RPCs) instead of the rigorous model (Grodecki, 2001). An advantage of using the RFM is that users are not required to know specific information about the satellite sensors. Furthermore, for a given elevation range, there is little difference in the projection accuracy of the RFM as opposed to the rigorous model (Grodecki, 2001). The basic RFM equation is developed in such a way that image coordinates can be computed from given ground coordinates. While the RFM equation is a nonlinear equation of 80 coefficients (RPCs), the RFM of 78 coefficients is often used because the first term in the denominator is usually set to one to avoid coefficient scale ambiguity.

Even though the provided RPCs' accuracy keeps improving with the development of precise orbit determination technology, there is still a need for postprocessing using actual or surrogate (secondary) ground control to achieve accurate georegistration. Note that the positional accuracy of typical RPCs provided by ground station data depends on the satellite and the terrain; the Kompsat-2 RPC error, for example, ranges up to hundreds of pixels.

The projection of airborne lidar point clouds to the HRSI space references the lidar points to the HRSI image coordinate system. Rasterization can be simply thought of as the filling of the empty image with lidar intensity return values. However, there are two minor issues associated with rasterization, namely, the presence of multiple lidar points on a single image pixel and the presence of holes (null points).

The projection of multiple lidar points onto the same image pixel can be expected because the lidar point density is usually higher than the HRSI spatial resolution. This becomes especially prominent along height breaklines, such as a building wall in a non-occlusion area, where the local point density increases enormously. An example of the multiple points-per-single-pixel problem near a building edge is depicted in Figure 2. Because of the elevation angle and azimuth of the HRSI imaging, some lidar points such as the solid square and star in Figure 2 fall within the HRSI occlusion area. On projection into the HRSI space, these occluded lidar points, whose positions differ, are referenced to the same image pixel. Ideally, these lidar points should not be projected because, in fact, they are not visible in the HRSI. To complicate matters, they will have different intensity return values; therefore, this effect should be avoided. A simple remedy is to select the lidar point having the highest elevation from among the points assigned to a single pixel during the rasterization process; these are the circle points in Figure 2. While this remedy may not be optimal where there are multiple lidar points over smooth terrain, it will not result in significantly poor rasterization because lidar data usually have higher spatial resolution than the HRSI.

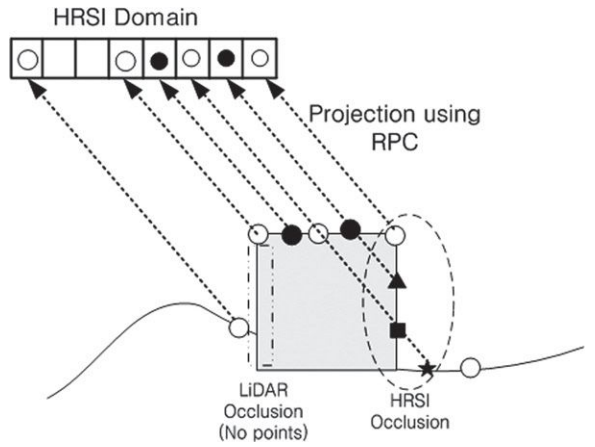

Figure 2. HRLI generation issues: multiple lidar points per pixel and the presence of holes in the HRSI space.

In contrast, the presence of a hole can occur, especially over areas of zero or low point density, mainly because of an irregular lidar point distribution caused by rugged terrain. Holes are also common at the side of a lidar strip because of the conventional line-scanner saw-tooth scan pattern. As shown in Figure 2, lidar occlusion areas lead to data-less pixels in the generated HRLI. These holes should be removed, because otherwise they will significantly disturb the edge extraction procedure. Application of the median filter is a popular but simple hole-removal method, although other filtering techniques such as a linear interpolation can be used. Figure 3 shows the result of median filtering of the image on the left to produce the image on the right, in which the holes have been successfully removed.

Edge information is extracted for matching from the generated HRLI. In this study, the well-known Canny-operator (Canny, 1986) is used because it is the most popular among the many edge extraction operators.

HRLI Patch Selection

The HRLI represents the incorrectly georegistered lidar intensity return image because it is generated using the provided RPCs, which are often erroneous. The goal is to perform image matching between the HRLI and HRSI for the determination of the RPC error.

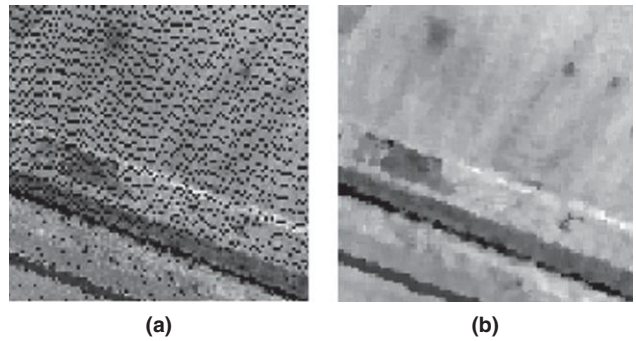

Figure 3. An example of applying the median filter to HRLI: (a) before (b) after (image size: 160 × 160 pixels).

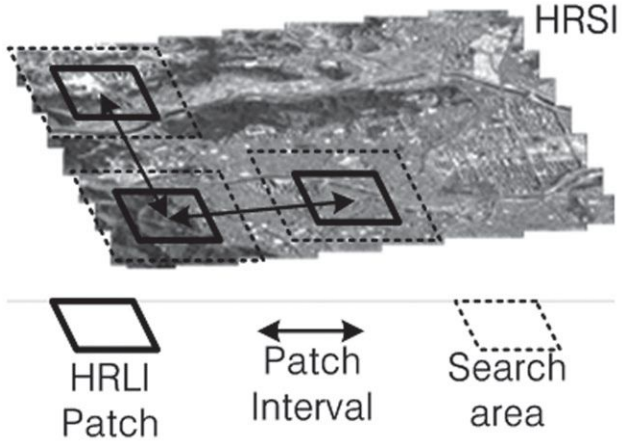

Figure 4. Representation of the patch size and interval.

The image matching is made for each HRLI image patch of a predefined size, taking into account the conventional error margin of the RPCs, which usually appears in the HRSI product-level specification. Figure 4 depicts the HRLI patch size relative to the HRSI search area, as well as the patch interval by which each patch is shifted in performing the search. Theoretically, a patch interval of a single pixel could be used for the search pattern. However, this is an inefficient and impractical search approach. It is important, therefore, to select both an efficient patch size and interval. For example, the patch size should be large enough to contain rich edge information for successful edge matching. Furthermore, a large patch size could guarantee a better matching success rate than a smaller patch, but it greatly increases the computational cost. The patch interval is directly related to the number of patches to be extracted from the HRLI; note that georegistration of HRSI requires a number of well-distributed control points over the entire image, e.g., more than 20 points for redundancy. Therefore, the use of a small patch interval can increase the number of matching points needed over the entire HRSI image to better estimate the georegistration parameters. However, note that this also affects the computational cost, in that a smaller patch interval will be computationally expensive, especially if combined with a large patch size.

Relative Edge Cross Correlation (RECC)

Lidar intensity returns differ significantly from HRSI spectral information, and this often leads to the failure of conventional spectral-based matching such as matching based on NCC. Also, there exists substantially heterogeneous edge information between HRLI and HRSI because of the different sensor characteristics. Consequently, the use of conventional edge-matching algorithms may require extensive postprocessing to reliably select meaningful edge information for matching. However, the underlying assumption of the study is that HRSI has a very narrow instantaneous field-of-view (IFOV), with a smooth trajectory that produces little geometric distortion, consisting mostly of a shift error. Moreover, it is assumed that the provided RPCs can serve as suitable constraints upon the search area. Therefore, the correct image location of the HRLI can be pinpointed, by moving the matching window to an area of the HRSI where there is both meaningful edge information and suitable HRSI/HRLI overlap. Based on this, the simple RECC edge similarity matching method is proposed. The method uses a relatively large window size consisting of hundreds of pixels designed to contain sufficiently high-quality edge similarity information between HRLI and HRSI. This edge similarity is measured using Equation 1, which computes the normalized number of overlapping edge pixels over the edge image of the HRLI and of the HRSI according to:

$$RECC = \frac{\sum_{i=1}^{r_1}\sum_{j=1}^{c_1} L_{ij} \times R_{ij}}{\sum_{i=1}^{r_1}\sum_{j=1}^{c_1} L_{ij} + \sum_{i=1}^{r_1}\sum_{j=1}^{c_1} R_{ij}} \quad (1)$$

where, *RECC* is relative edge cross correlation, L is an edge image of the HRLI patch, R is an edge image of a sub-array of the HRSI, and L_{ij} and R_{ij} are the digital numbers associated with image L and image R, respectively, at line i and sample j (this digital number is one if it is on the edge, otherwise it is zero). Therefore, if an edge pixel exists in both images, $L_{ij} \times R_{ij}$ will be one; otherwise, it will be zero. The numerator is the sum of the pixels and the denominator is the total number of edge pixels that appear in the two images.

Equation 1 is similar to the well-known NCC matching equation and can be computed by using a computationally expensive moving window over the region of interest (ROI). This computational cost can be significantly reduced if the following two terms are computed using the convolution theorem in the frequency domain. The summation in Equation 2 can be computed by convolving the HRSI with a window all of whose elements are one. Multiplication and summation in Equation 3 can be performed by multiplying Fourier-transformed images of HRLI and HRSI, $F(L)$ and $F(R)$, respectively, followed by its inverse Fourier transform.

$$\sum_{i=1}^{r_1}\sum_{j=1}^{c_1} R_{ij} \quad (2)$$

$$\sum_{i=1}^{r_1}\sum_{j=1}^{c_1} L_{ij} \times R_{ij} \quad (3)$$

Note that the RECC value is an indicator of relative matching among the candidate matching points in the ROI. Since the number of edge pixels, which is the denominator of Equation 1, can vary depending on the scene contrast, the RECC value will also vary. Therefore, there should be another step to determine if a RECC value indicates reliable matching. However, unlike NCC for which the usual threshold is 0.75, it is not possible to establish a RECC threshold value. This situation impacts upon effective edge matching, which ideally should be minimally affected by outliers.

One usually assumes a unique corresponding matching point in the reference image; however, this is not true in the case of this application. Figure 5 shows the computed RECC values around a region of maximum RECCs in a region that differs significantly from its surrounding values. It indicates that, for this test data, the edge matching is successful for both the line and the sample direction. Note that the image center of the HRSI of Figure 5 represents the initial search location, and the "x" mark with the surrounding box is the matched position. Figure 6 is an example of the RECC value distribution for a different data set. Note that edge information in these images is not very distinct. In contrast to the previous example, this distribution demonstrates a more uniform array of RECC values around the maximum value in both the line and the sample direction. Therefore, this matching result cannot be trusted even though the maximum value can be obtained.

In this regard, the CV can be a useful indicator of the edge matching. CV is determined by a simple computation performed by averaging distances from the maximum RECC

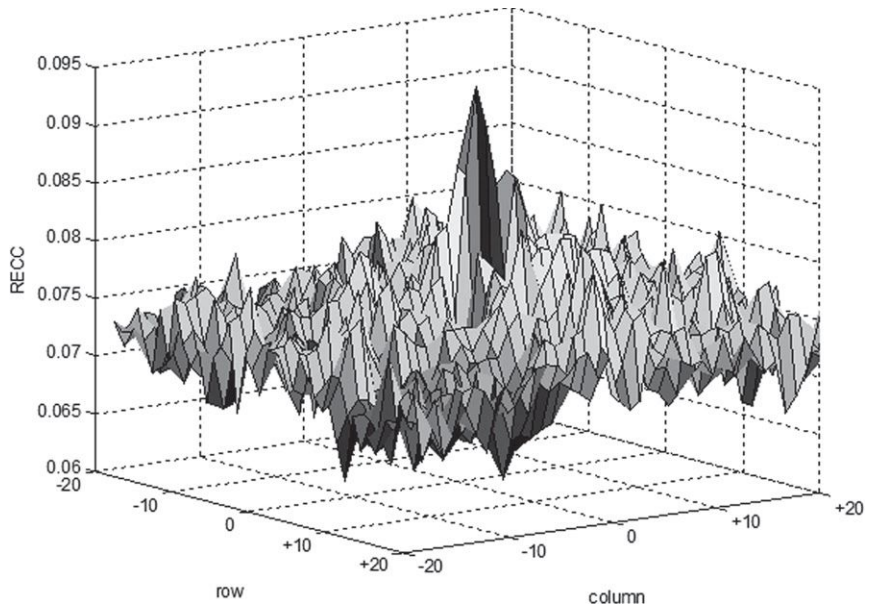

(a)

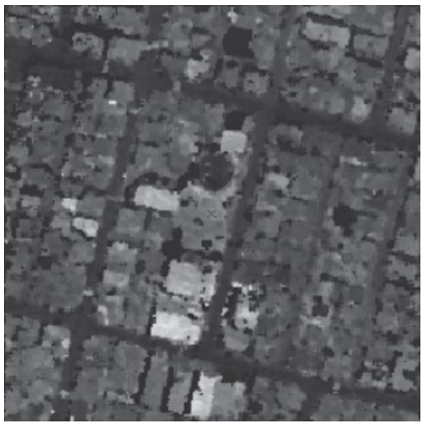

(b)

(c)

Figure 5. A RECC distribution around the maximum showing (a) good matching, (b) HRLI, and (c) HRSI.

to subsequent RECC values starting at the next highest until the n^{th} (in decreasing order) maximum value, as defined in Equation 4:

$$CV_n = \frac{\sum_{i=1}^{n} \sqrt{(r_{\max} - r_i)^2 + (c_{\max} - c_i)^2}}{n} \quad (4)$$

where CV_n is the concentration value based on the maximum to n^{th} largest RECC values, and $(r_{\max}, c_{\max})$ and (r_i, c_i) are the image coordinates of the positions of the maximum RECC and i^{th} largest RECC values, respectively.

A smaller CV means that prominent RECC peak values are concentrated in a small region and it indicates a high possibility of correct matching. In contrast, a higher CV means that peak RECC values are sparsely distributed and that it is difficult to select a prominent RECC peak point. For example, in Figure 5, the average distance from the maximum peak to the next four peaks (CV_4) is 1.1 pixels such that the maximum peak can be easily distinguished, and, hence, it represents a reliable matching point. In contrast, in Figure 6, CV_4 is 53.2 pixels, indicating that it is difficult to determine which peak represents a reliable matching location.

An experiment was carried out to show the feasibility of using the CV as a threshold for RECC matching. The RECC image matching error was computed for over 200 matching points between the HRLI and HRSI by comparing with the correct matching positions, and the error is plotted for RECC and CV as shown in Figure 7. First, the RECC versus error graph shows that the RECC is not highly related to matching accuracy. A large RECC seems to show great accuracy when there are only a few matching points, which is at the expense of the redundancy needed for automated georegistration. Note that most of the good matching points have RECC values in the range of 0.06 to 0.09, and these are not

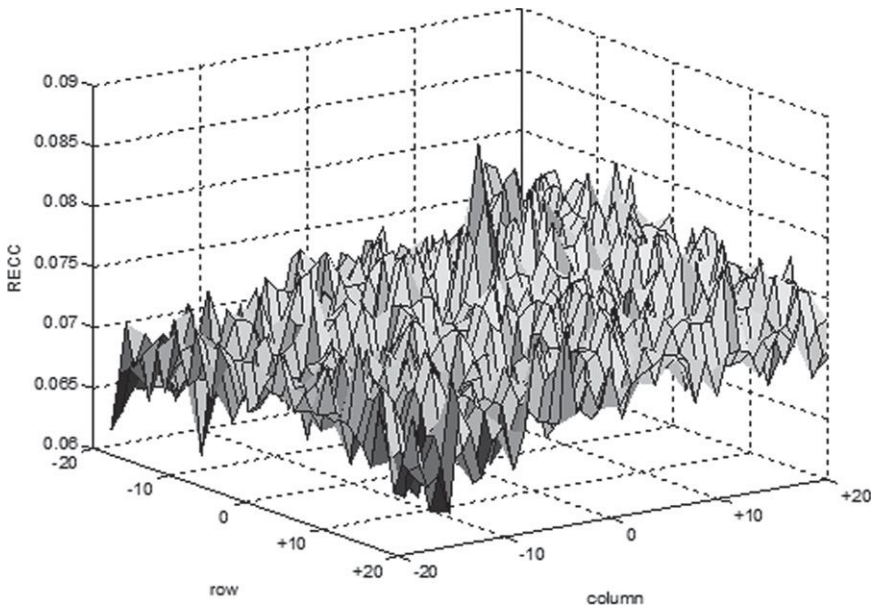

(a)

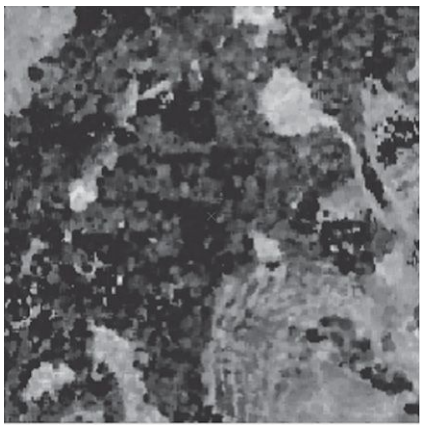

(b)

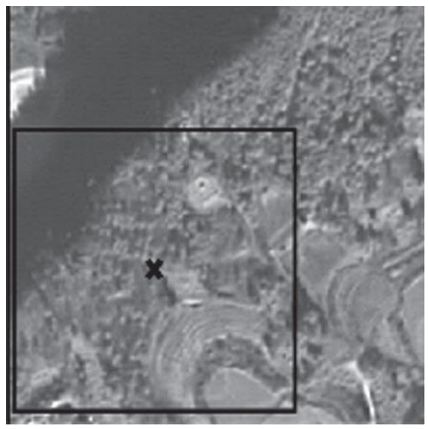

(c)

Figure 6. A RECC distribution around the maximum showing that (a) the matching cannot be trusted, (b) HRLI, and (c) HRSI.

suitable indicators by which to successfully filter out inaccurate image matching. It can be concluded, therefore, that it is not reasonable to use a high RECC value as a threshold to remove low accuracy matching. Second, the CV versus error plot shows that most of the highly accurate matching points have small CVs. This indicates that using a small CV as a threshold to remove outlier matching can secure both redundancy and high accuracy, even if a small CV still cannot guarantee an outlier-free situation, and requires a final outlier check process.

Finally, the well-known image-matching techniques such as NCC and scale-invariant feature transform (SIFT) (Lowe, 1999) were attempted in order to match the HRLI and HRSI. These results were compared to the RECC matching. A built-up area was selected for the test to ensure the inclusion of rich feature information, as shown in Figure 8. This figure shows the matching results of the SIFT and RECC techniques. The NCC did not provide any successful matching points. In other words, all the correlation values were smaller than the threshold 0.75. SIFT provided only two matching points, which, unfortunately, were incorrect. The test results clearly show that the NCC and SIFT techniques did not effectively handle the spectral difference between the HRLI and HRSI.

Georegistration Model with Outlier Removal

Since the georegistration problem is simplified to a 2D case for the shift, well-known affine and second-order polynomial models can be used as indicated in Equation 5, where the second-order coefficients are set to zero for the affine model and only a_1 and b_1 are used for the shift model:

$$s' = a_1 + a_2 s + a_3 l + a_4 s^2 + a_5 sl + a_6 l^2$$
$$l' = b_1 + b_2 s + b_3 l + b_4 s^2 + b_5 sl + b_6 l^2 \quad (5)$$

where, s, l are the original image coordinates of the conjugate points (sample and line) and s', l' are the georegistered coordinates of the conjugate points.

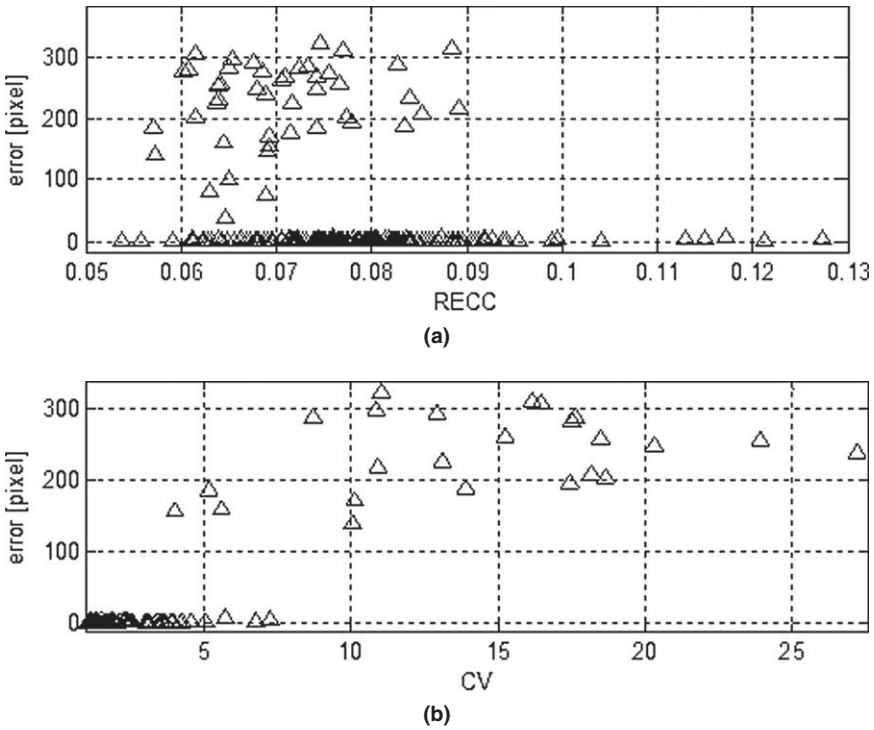

Figure 7. Image matching error (pixels) as a function of (a) RECC, and (b) CV (the triangles show the error for 200 matching points).

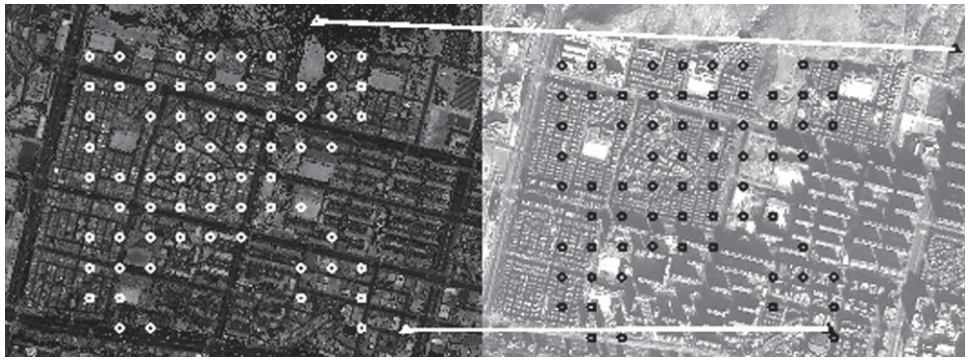

(a) (b)

Figure 8. RECC and SIFT test results for image-matching comparison between (a) HRLI, and (b) HRSI (circles: RECC results; triangles and connecting lines: SIFT results).

Even though RECC with CV should be highly resistant to outlier influence, the existence of outliers after this stage is still a concern. This study therefore employs Baarda's data snooping method as a safeguard against additional undetected outliers infecting the georegistration problem. For details, refer to Baarda (1968).

Experiment

Data

Three Kompsat-2 images were tested for the proposed method. Table 1 shows the specification of each image. Kompsat-2 data have 15,000 pixels per line and a ground sample distance (GSD) of about one meter. The test target area is Daegu, Korea, located at about 35.89°N and 128.49°E, where the highest terrain elevation is about 400 m ASL. A number of ground checkpoints were acquired from stereo aerial images over the entire area for the purpose of accuracy assessment. Figure 9 depicts the distribution of checkpoints. Note that the image coordinate error of the provided RPCs was estimated to be in the range of 31 to 146 pixels for the checkpoints.

HRLI Generation

Airborne lidar data were projected to the HRSI space and rasterized for the HRLI. Note that HRLI has the same one-meter spatial resolution as HRSI. Figure 10 is the generated

TABLE 1. SPECIFICATION OF KOMPSAT-2 TEST DATA

Image number	No. 1	No. 2	No. 3
Acquisition date	01/03/2009, 01:34	12/312009, 01:19	02/07/2010, 01:07
Incidence/Azimuth	6.2°/249.1°	14.1°/256.1°	5.8°/91.7°
Ground Sampling Distance (line/sample)	1.004/1.003 m	1.050/1.031 m	0.981/0.988 m
Image size (line/sample)	15,500 × 15,000	15,500 × 15,000	15,500 × 15,000
No. of checkpoints	86	81	86
RPCs mean error [pixels] (sample/line)	41.40/31.49	64.67/135.76	29.34/146.43

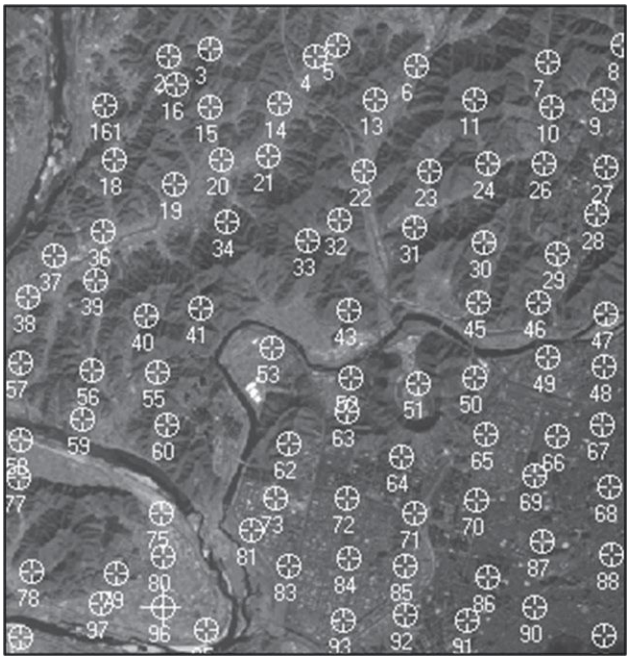

Figure 9. Kompsat-2 data with checkpoint distribution.

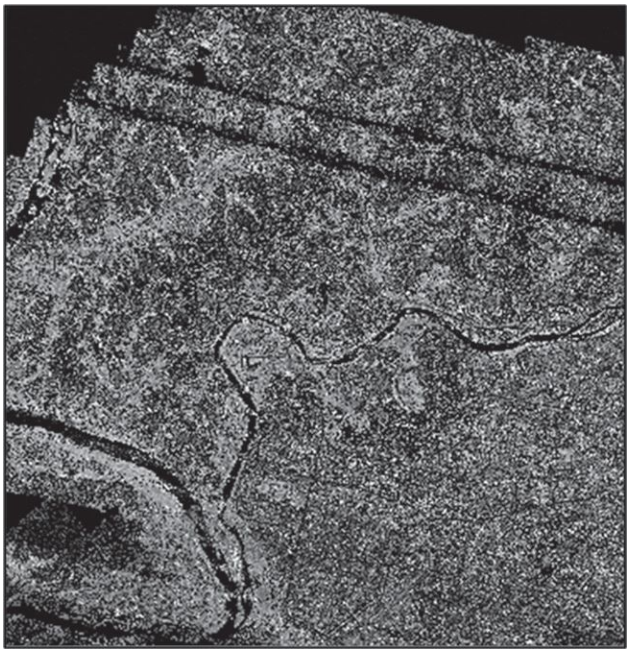

Figure 10. Generated HRLI showing some data voids.

HRLI showing some data voids at the upper-left, upper-right, and lower-left corners. Some additional data voids exist in other parts of the image, especially in the upper side where data voids along the lidar strips are observed, mostly because of a lack of lidar strip overlap.

Analysis on Patch Size and Interval

The proposed matching technique was first tested for image No. 1 by changing the patch size and interval. The number of matching points was counted, as presented in Figure 11. In performing the RECC matching, a CV_4 threshold of 1.5 pixels was used. As expected, a larger patch size tends to yield more matching points, but it is also more computationally expensive. On the other hand, a small patch size such as, 100 × 100 pixels did not seem to provide a good number of matching points. Note that the patch size should be large enough to contain rich edge information. Also, as the patch interval increases, the number of matches decreases. Patch intervals of 3,000 and 4,000 pixels that yield less than 20 points may not be redundant for modeling the affine and polynomial-based entire image transformation. To ensure redundancy in the number of matching points throughout the image, a smaller interval is preferred, but it should be noted that a smaller interval requires a higher computational cost. To obtain a reasonable number of matching points, more than 20 over the entire image, for example, a patch

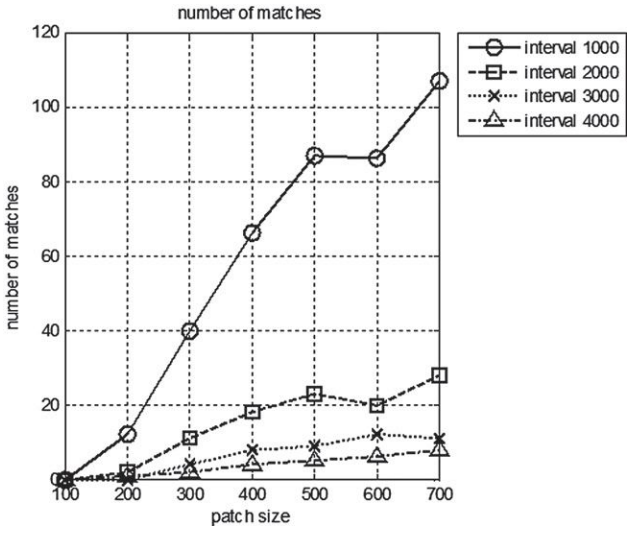

Figure 11. Relationship of the number of matching points to the patch size and patch interval for RECC with CV 1.5 pixels (image No. 1).

interval of less than 2,000 pixels, with a patch size of more than 400 × 400 pixels, should be used.

Affine and polynomial parameters were estimated and their accuracy computed using checkpoints from the matching test results. The mean errors were computed and are plotted in Figure 12. The error tends to decrease as patch size increases and as the patch interval decreases. The accuracy seems to stabilize from a patch size of 400 × 400 pixels or 500 × 500 pixels. Note that the horizontal error of 1.4 pixels corresponds to about one-pixel accuracy in each line and sample direction. No outlier was detected in the final outlier-detection process, indicating that the proposed RECC matching was deemed reliable. A larger patch interval, which yields a smaller number of matching points, would not be adequate to estimate polynomial parameters because the polynomial model has more parameters than the affine model. A smaller patch interval (such as, 1,000 pixels) yields the most stable accuracy. Therefore, overall, a patch size of 500 × 500 pixels, with an interval of 1,000 pixels was deemed to yield the best results for the data set. However, it should be noted that these optimal numbers may not work for a different data set.

CV Threshold

Six different CV_4 thresholds were tested using a 500-pixel patch size and a 1,000-pixel interval to explore the number of matches and matching accuracy, as presented in Figure 13. Figure 13a shows that the number of matches tends to increase as the threshold is increased. In Figure 13b, before outlier removal was performed, CV_4 thresholds of 1.5, 2, 3, and 4 pixels yielded a similar accuracy of about one pixel in each sample and line direction. However, the matching accuracy worsened for threshold values of 5 and 6 pixels. When the outlier detection based on Baarda's data snooping was applied, one and four outliers were detected where the CV_4 threshold values of 5 and 6 pixels, respectively, were used. As can be seen from Figure 13b, by removing these outliers, matching accuracy improved significantly. However, as long as the redundancy in the estimation is sufficient, there is no reason to increase the threshold limit.

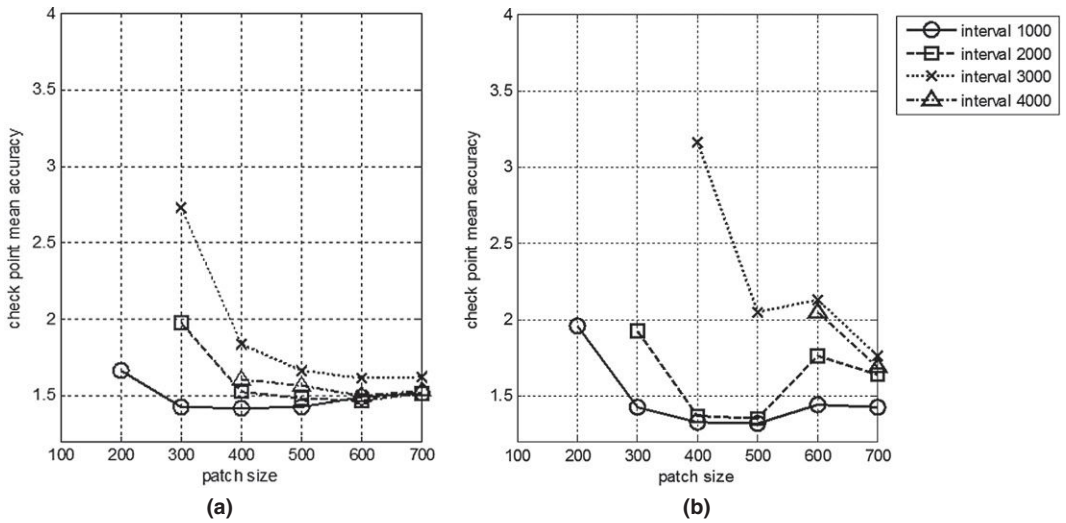

Figure 12. Georegistration accuracy versus the patch size and patch interval (based on Image No. 1) for the (a) affine model, and (b) second order polynomial.

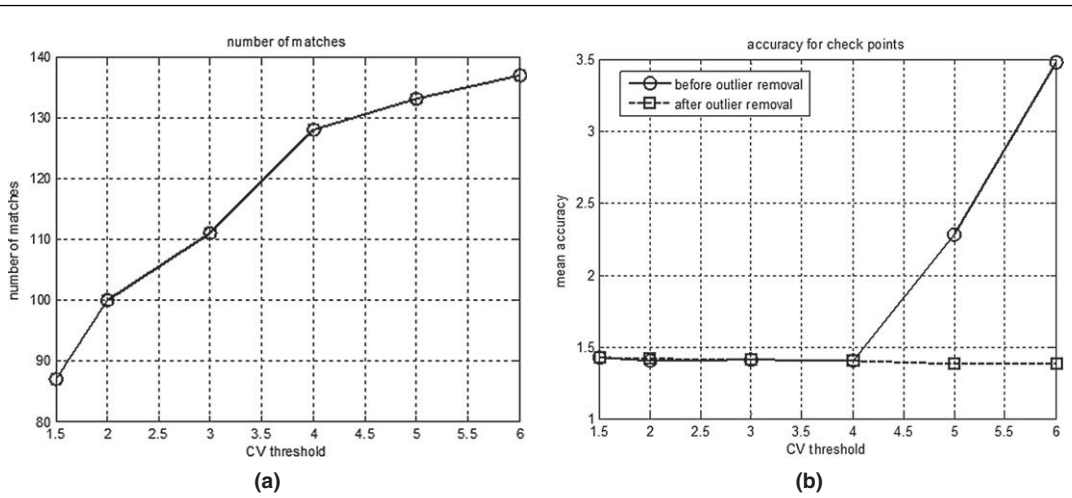

Figure 13. Effect of the CV_4 threshold on (a) number of matching points and (b) mean accuracy.

TABLE 2. AUTOMATIC GEOREGISTRATION ACCURACY (UNIT: PIXEL)

Image	Model	Before outlier removal		After outlier removal	
		Mean (sample/line)	Max (sample/line)	Mean (sample/line)	Max (sample/line)
No. 1	Shift	0.83 / 4.35	2.90 / 10.86	–	
	Affine	0.90 / 1.10	3.44 / 4.31	–	
	Polynomial	0.85 / 1.01	3.55 / 4.25	–	
No. 2	Shift	1.05 / 4.05	3.62 / 8.59	–	
	Affine	1.06 / 1.02	5.39 / 3.83	0.83 / 1.01	3.61 / 3.81
	Polynomial	1.13 / 0.95	5.64 / 4.20	0.77 / 0.95	3.24 / 4.19
No. 3	Shift	0.84 / 4.67	3.40 / 11.99	–	
	Affine	0.72 / 0.94	2.81 / 3.14	–	
	Polynomial	0.70 / 0.89	2.27 / 3.19	–	

Automatic Georegistration based on the Proposed Method

Based on the analysis carried out previously, HRSI georegistration of the tested Kompsat-2 images was performed using a 500 × 500 pixel patch size, 1,000-pixel interval, and a CV_4 threshold of 1.5 pixels. Table 2 presents the georegistration accuracy results generated from the checkpoints for three different transformation models, namely, a shift, affine and second-order polynomial model.

When only shift parameters (a_1, b_1) were estimated, large errors were observed, especially in the line direction. In the case of images No. 1 and No. 3, the affine and polynomial models provided much better accuracy and the mean accuracy was bounded at the sub-pixel level in the line and sample directions. Note that no outlier among the matched points was indicated for the images No. 1 and No. 3 such that all the matched points were kept. However, in the case of image No. 2, six outlier matched points were detected and removed at a confidence level of 99 percent. After removing them, the mean accuracy dropped to a sub-pixel level.

Figure 14 depicts the location of patches and checkpoint errors in image No. 2. The figure also shows which patches were successfully matched and which were removed as outliers. Note that the patches are well distributed over the entire image area, except where the lidar data are missing. When the HRLI was overlaid over image No. 2, it was found that all of the outlier patches were located along the lidar strip for which there was little lidar strip overlap. The authors feel that the ground accuracy of the lidar strip is relatively low when compared with conventional lidar accuracy, especially in an east/west direction, because of the inaccurate strip adjustment. In the case of images No. 1 and No. 3, the dubious lidar strip did not yield any successful matching. This lidar strip will have to be checked with the checkpoints or with additional field surveys.

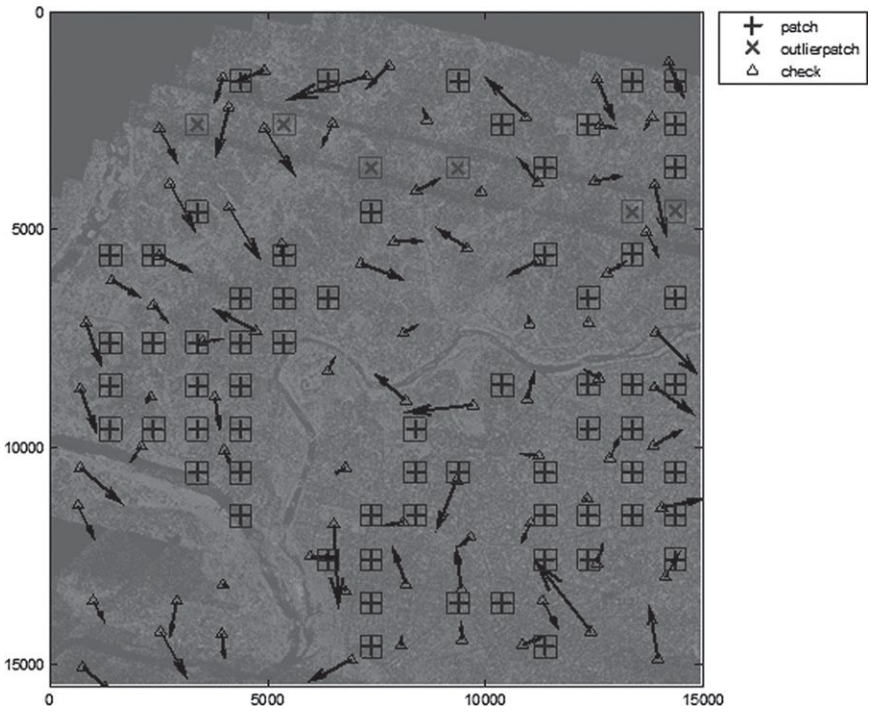

Figure 14. The patches removed as outliers in image No. 2.

Summary and Conclusions

This study proposes a new method for automatic refinement of HRSI RPC using airborne lidar intensity return information. The proposed approach was developed based on the attractive properties of high point density, accuracy, and the relief displacement-free characteristics of airborne lidar point clouds. Lidar intensity return information is first projected into the HRSI space using RPC and rasterized for HRLI. Note that the difference between the HRLI and HRSI indicates the georegistration error of the RPC. This difference is determined over the entire image by the FFT-based RECC and CV to overcome the spectral differences. Finally, the rigorous Baarda's data snooping outlier-removal process is carried out for the final check of outliers.

Experiments were carried out for three Kompsat-2 images over the Daegu area in South Korea. Before applying the proposed method to the dataset, well-known image-matching techniques such as NCC and SIFT were tested to show the ability of the proposed matching method to handle high spectral differences. Detailed analysis of the RECC matching patch and CV parameters was then carried out to determine the optimal matching patch size, interval, and CV threshold. Based on the analysis, 500 $\times$ 500 pixels of patch size, 1,000 pixels of interval, and 1.5 pixels of CV threshold were selected. From the RECC matching with the parameters, a number of matches were obtained for the entire Kompsat-2 image region. The rigorous outlier-removal process in the RPC refinement could capture and locate the inaccurate matching points that were located along a dubious lidar strip. After removing them, the RPC could be refined to a sub-pixel level of accuracy, showing the potential of the proposed methodology.

Future work will include more experiments on diverse HRSI over different terrains. More extensive performance comparisons of the method will need to be applied to the conventional automated georegistration methods. We also recommend analysis of the effects of the object space conditions such as the texture content when making the selection of an optimal matching patch size.

Acknowledgments

This work was supported by the National Research Foundation of Korea Grant funded by the Korean Government (NRF-2010-013-D00072).

References

Abedini, A., M. Hahn, and F. Samadzadegan, 2008. An investigation into the registration of LIDAR intensity data and aerial images using the SIFT approach, *International Archives of the Photogrammetry, Remote Sensing and Spatial Information Sciences*, 37(B1):169–174.

Baarda, W., 1968. A testing procedure for use in geodetic networks, *Netherlands Geodetic Commission, Publications on Geodesy, New Series*, Delft, 2(5):27–30.

Bentoutou, Y., N. Taleb, K. Kpalma, and J. Ronsin, 2005. An automatic image registration for applications in remote sensing, *IEEE Transactions on Geoscience and Remote Sensing*, 3(9):2127–2137.

Canny, J.F., 1986. A computational approach to edge detection, *IEEE Transactions on Pattern Analysis and Machine Intelligence*, 8:679–698.

Cariou, C., and K. Chehdi, 2008. Automatic georeferencing of airborne pushbroom scanner images with missing ancillary data using mutual information, *IEEE Transactions on Geoscience and Remote Sensing*, 46(5):1290–1300.

Chen, H.M., M.K. Arora, and P.K. Varshney, 2003. Mutual information-based image registration for remote sensing data, *International Journal of Remote Sensing*, 24(18):3701–3706.

Choi, K.A., J.S. Hong, and I.P. Lee, 2011. Precise geometric registration of aerial imagery and LIDAR data, *ETRI Journal,* 33(4):506–516.

Dial, G., and J. Grodecki, 2002. Block adjustment with rational polynomial camera models, *Proceedings of the ACSM-ASPRS 2002 Annual Conference*, Washington D.C., 22–26 April, unpaginated CD-ROM.

Dowman, I.J., A. Morgado, and V. Vohra, 1996. Automatic registration of images with maps using polygonal features, *International Archives of Photogrammetry and Remote Sensing*, 31(B3): 139–145.

Fonseca, L.M.G., and B.S. Manjunath, 1996. Registration techniques for multisensor remotely sensed imagery, *Photogrammetric Engineering & Remote Sensing*, 62(9):1049–1056.

Fraser, C.S., and H.B. Hanley, 2005. Bias-compensated RPCs for sensor orientation of high-resolution satellite imagery, *Photogrammetric Engineering & Remote Sensing*, 71(8): 909–915.

Grodecki, J., 2001. IKONOS stereo feature extraction - RPCs approach, *Proceedings of the ASPRS 2001 Annual Convention*, St. Louis, Missouri, 25-27 April, unpaginated CD-ROM.

Guo, T., and Y. Yasuoka, 2002. Snake-based approach for building extraction from high-resolution satellite images and height data in urban areas, *Proceedings of the 23rd Asian Conference on Remote Sensing*, Kathmandu, unpaginated CD-ROM.

Habib, A.F., G. Mwafag, M. Morgan, and R. Al-Ruzouq, 2005. Photogrammetric and LIDAR data registration using linear features, *Photogrammetric Engineering & Remote Sensing*, 71(6): 699–707.

Hild, H., 2001. Automatic image-to-map-registration of remote sensing data, *PhotogrammetrischeWoche*, URL: *http://elib.uni-stuttgart.de/opus/volltexte/2001/966/*, (last date accessed: 06 July 2012).

Kim, T., and Y. Im, 2003. Automatic satellite image registration by combination of matching and random sample consensus, *IEEE Transactions on Geoscience and Remote Sensing*, 41(5):1111–1117.

Kim, J.R., and J. P. Muller, 2002. 3D reconstruction from very high resolution satellite stereo and its application to object identification, *International Archives of Photogrammetry, Remote Sensing and Spatial Information Sciences*, Vol. 34 (Part 4), unpaginated CD-ROM.

Lee, D.C., J.H. Yom, S.W. Shin, J.H. Oh, and K.S. Park, 2011. Automatic building reconstruction with satellite images and digital maps, *ETRI Journal,* 33(4):537–546.

Lee, J., C. Lee, and K. Yu, 2011. Autoregistration of high-resolution satellite imagery using LIDAR intensity data, *KSCE Journal of Civil Engineering*, 15(2):375–384.

Li, Q., G. Wang, J. Liu, and S. Chen, 2009. Robust scale-invariant feature matching for remote sensing image registration, *IEEE Geoscience and Remote Sensing Letters*, 6(2):287–291.

Lowe, D.G., 1999. Object recognition from local scale-invariant features, *Proceedings of the International Conferences on Computer Vision*, Corfu, Greece, pp.1150–1157.

Mwafag, G., 2006. *Integration of Photogrammetry and LIDAR*, Ph.D. dissertation, University of Calgary, Calgary, Alberta, Canada.

Moigne, J.L., A. Cole-Rhodes, R. Eastman, P. Jain, A. Joshua, N. Memarsadeghi, D. Mount, N. Netanyahu, J. Morisette, and E. Uko-Ozoro, 2006. Image registration and fusion studies for the integration of multiple remote sensing data, *Proceedings of the 2006 IEEE International Conference on Acoustics, Speech and Signal Processing*, 5:1189–1192.

Oh, J.H., W.H. Lee, C.K. Toth, D.A. Grejner-Brzezinska, and C.N. Lee, 2010. A piecewise approach to epipolar resampling of pushbroom satellite images based on RPC, *Photogrammetric Engineering & Remote Sensing*, 76(12):1353-1363.

Oh, J.H., C. K. Toth, and D.A. Grejner-Brzezinska, 2011. Automatic geo-referencing of aerial images using high-resolution stereo satellite images, *Photogrammetric Engineering & Remote Sensing*, 77(11):1157-1168.

Schickler, W., 1994. Feature matching for outer orientation of single images using 3-D wireframe control points, *International Archives of Photogrammetry and Remote Sensing*, 29:591–598.

Shi, W., and A. Shaker, 2006. The line-based transformation model (LBTM) for image-to-image registration of high-resolution satellite image data, *International Journal of Remote Sensing*, 27(14):3001– 012.

Sohn, G., and I. Dowman, 2007. Data fusion of high-resolution satellite imagery and LiDAR data for automatic building extraction, *ISPRS Journal of Photogrammetry and Remote Sensing*, 62(1):43–63.

Stoker, J., D. Harding, and J. Parrish., 2008. The need for a national lidar dataset, *Photogrammetric Engineering & Remote Sensing*, 74(9):1066–1068.

Ton, J., and A.K. Jain, 1989. Registering Landsat images by point matching, *IEEE Transactions on Geoscience and Remote Sensing*, 27(5):642–651.

Wong, A., and D.A. Clausi, 2007. ARRSI: Automatic registration of remote-sensing images, *IEEE Transactions on Geoscience and Remote Sensing*, 45(5):1483–1493.

Zhang, Z., J. Zhang, M. Liao, and L. Zhang, 2000. Automatic registration of multi-source imagery based on global image matching, *Photogrammetric Engineering & Remote Sensing*, 66(5):625–629.

(Received 19 August 2011; accepted 03 December 2011; final version 13 March 2012)